J Mater Sci (2010) 45:2408–2418
DOI 10.1007/s10853-010-4208-y

Determination of the elastic modulus of highly porous samples by nanoindentation: a case study on sea urchin spines

Volker Presser · Karin Gerlach · Achim Vohrer · Klaus G. Nickel · Werner F. Dreher

Received: 22 August 2009 / Accepted: 5 January 2010 / Published online: 20 January 2010

Abstract Nanoindenation studies were carried out on single crystal calcite and on sea urchin spines from *Heterocentrotus mammillatus*, *Phyllacanthus imperialis*, and *Prinocidaris baculosa*. Unlike dense calcite single crystals resin embedded porous sea urchin spine segments showed a strong dependence of the indentation modulus, but not the indentation hardness, on the local porosity. This implies that the sampled volume for the indentation modulus in nanoindentation with forces down to 15 mN is not nanoscopic but extends approximately 50 μm around the indentation spot. Only for indentation depths $\ll$100 nm more or less mount-unaffected values of the indentation modulus could be found. The Voigt model for composite materials (calcite/resin) was found to be applicable for the dependency of the indentation modulus on the porosity. This is attributed to the network type of porosity and opens strategies for the control of stiffness in porous networks.

Introduction

Nanoindentation, also referred to as load and depth-sensing indentation (DSI), has become a very important method to study the mechanical properties on the (sub)micrometer scale [1–4], which was successfully adapted even to layered and thin film systems [2, 3].

The basis for DSI is the interpretation of in situ loading–unloading curves. Mechanical sample properties such as indentation hardness (H_{IT}) and indentation modulus (E_{IT}) can easily be derived from load–displacement plots. Under ideal conditions, the indentation modulus E_{IT} is equal (or, at least, similar) to the Young's modulus as obtained, for example, via bending tests [4].

Continuous stiffness measurement (CSM) allows obtaining depth-resolved values for the indentation hardness and the elastic modulus [5]. Here a sine modulation superimposes the loading path so that material properties like hardness and indentation modulus can be obtained in a continuous way from the displacement oscillation [6]. This way, surface hardening due to mechanical treatment or the transition from the layer- to the substrate-dominated domain in thin film systems can be analyzed [5, 7]. There are, however, severe complications in interpretation of the obtained data for samples with a high modulus to hardness ratio (E/H): Copper or nickel single crystals ($E/H > 200$) were demonstrated to yield high errors in calculated values due to a large contribution of dynamic unloading [8, 9]. This effect is less important for calcite ($E/H = 30$–40) [10, 11].

This study was motivated by the high biomimetic potential of sea urchin spines, which show a beneficial cascading graceful failure fracture behavior under compression [12, 13]. It is possible to correlate this beneficial behavior with the microstructure of mesocrystalline magnesium calcite (referred to as the stereom) where more dense areas enable crack deflection. In addition, we find some minor organic components in the stereom in-between the Mg–calcite nanodomains [14–19]. As compression or

V. Presser (✉) · K. G. Nickel
IFG Institute for Geoscience, Eberhard-Karls-Universität, Wilhelmstraße 56, 72074 Tübingen, Germany
e-mail: volker.presser@uni-tuebingen.de

K. Gerlach · W. F. Dreher
NMI Natural and Medical Sciences Institute at the University of Tübingen, Markwiesenstraße 55, 72770 Reutlingen, Germany

A. Vohrer
Institute of Textile Technology and Process Engineering Denkendorf (ITV), Körschtalstraße 26, 73770 Denkendorf, Germany

Table 1 E_{IT} and H_{IT} values as obtained from DSI experiments (15 mN) on sea urchin spines

Sea urchin species	Measured area description	Number of indentations	E_{IT} (GPa)	H_{IT} (GPa)	Porosity (vol%)
Heterocentrotus mammillatus	Growth ring 1	13	61.9 ± 2.7	3.7 ± 0.3	17 ± 2.2
	Growth ring 2	18	62.6 ± 3.7	3.4 ± 0.4	19 ± 2.4
	Growth ring 3	18	60.9 ± 4.0	3.5 ± 0.3	16 ± 1.9
	Growth ring 4	15	61.5 ± 3.9	3.4 ± 0.4	20 ± 2.3
	Outer porous area	13	50.5 ± 3.0	3.3 ± 0.3	38 ± 3.1
	Inner porous area	8	39.8 ± 6.1	3.1 ± 0.4	61 ± 4.8
Phyllacanthus imperialis	Outer porous area	15	48.4 ± 4.2	4.0 ± 0.3	40 ± 2.7
	Middle porous area	24	46.9 ± 5.1	4.0 ± 0.5	45 ± 4.1
	Inner porous area	6	28.9 ± 5.8	2.8 ± 0.8	71 ± 3.4
Prinocidaris baculosa	Porous outer part	15	59.1 ± 5.0	3.9 ± 0.4	25 ± 2.8
	Massive outer part	15	71.7 ± 3.8	3.5 ± 0.2	8 ± 1.8
	Outer porous part	21	52.8 ± 7.8	3.7 ± 0.5	37 ± 3.6
	Inner porous part	15	48.5 ± 5.7	3.5 ± 0.5	48 ± 5.5

For the nomenclature see also Fig. 2

bending tests only yield information on the entire sample comprising several levels of porosity, nanoindentation was applied to closer investigate elastic modulus and hardness as properties of the basic calcite. Highly porous spines of three different sea urchins were investigated: *Heterocentrotus mammillatus* (HM), *Phyllacanthus imperialis* (PI), and *Prinocidaris baculosa* (PB).

Various studies and standards comment the critical influence of the mounting material on the determined mechanical sample properties [5, 9, 20]. Unlike other studies, where dense samples were used, sample polishing and treatment of sea urchin spines required infiltrating and mounting the samples with resin. This study describes the effects of resin mounting and infiltration on the results of nanoindentation experiments including depth-resolved measurements using the CSM technique and hereby explores the sample volume (Table 1).

Experimental

DSI and CSM measurements were carried out via a Nano-Hardness Tester® from CSM Instruments SA (Peseux, Switzerland) with a Berkovich diamond indenter. For all calculations, the model of Oliver and Pharr [6] was used for data interpretation. The use of a sapphire reference ring compensated for load frame compliance and thermal drift and also provided shielding from external influences such as fluctuations of the atmospheric pressure, humidity, and so on. Both loading and unloading were performed with 9 mN/min and a maximum load of 15 mN which was maintained for 30 s. This holding time is the same as used in a recent study on brachiopod calcite [21]. For the two modes of CSMs, a sine frequency of 20 Hz (1 Hz) was used which corresponds to an amplitude of 5 mN (1 mN). Loading and unloading were carried out with 50 mN/min (7.5 mN/min) and a maximum load of 50 mN (20 mN), which was also maintained for 30 s.

Porous sea urchin spine samples from *Heterocentrotus mammillatus*, *Phyllacanthus imperialis*, and *Prinocidaris baculosa* were used. All samples and all measured sample positions showed almost the same chemical composition of Calcite ($CaCO_3$) with ca. 2 wt% Mg as determined via EDX. For DSI measurements, the samples were embedded in and, thereby, infiltrated with epoxy resin (Spezifix-20®; Stuers GmbH, Germany). DSI measurements yielded for the resin $E_{IT} = 3.6 \pm 0.1$ GPa and $H_{IT} = 198 \pm 4$ MPa. The mechanical properties of the resin are important for the interpretation of the calculated Young's modulus of the resin-infiltrated porous samples.

Creep within the specimen C_{IT} was observed when the maximum force was maintained for 30 s for both CSM and static loading mode. C_{IT} was calculated after Eq. 1 [4] to range between 1.0 and 1.7% for all samples.

$$C_{IT} = \frac{h_2 - h_1}{h_1} \cdot 100\% \quad (1)$$

In addition to DSI measurements, conventional bending tests were performed to determine the elastic modulus of entire sea urchin spine samples ($4.0 \times 4.0 \times 44.5$ mm^3). Conventional three-point bending tests were performed using a universal testing machine (Instron 4502, Instron Deutschland GmbH, Germany) with a constant crosshead movement speed of 0.5 mm/min. For the lower mounting a distance of 40 mm between the supporting bearings was chosen while the upper and one of the lower bearings rested on a spherical support. This allowed the mount to

align ideally to the sample without inducing misalignment-related stress to the sample's edges.

Microscopic investigations of the samples were carried out using an Olympus BH-2 Nomarski Differential Interference Contrast (DIC) microscope (Olympus Europa GmbH, Germany). For image analysis we followed the stereological approach based on Delesse and Rosiwal [22, 23] (area fraction of phase A = volume fraction of phase A) and used ImageJ 1.42 (National Institutes of Health, United States of America).

Results

Three-point bending test

Three-point bending tests were carried out on a cuboid sample ($4 \times 4 \times 45$ mm^3) cut from a spine of *Heterocentrotus mammillatus*. Catastrophic sample failure was avoided by applying maximum forces below the critical bending strength. Data from both loading and unloading curves were used to determine the elastic modulus via Eq. 2

$$E_{\text{three-point bending}} = \frac{\varepsilon \cdot L^3}{4w \cdot h^3} \tag{2}$$

In Eq. 2, ε denotes the slope in the force–deflection plot ($\mathrm{d}F/\mathrm{d}x$) in the linear domain and L the distance between the lower bearings ($L = 40.0$ mm). Finally, w and h stand for the width (w) and the height (h) of the sample ($w = h = 4.0$ mm).

As a result for two loading–unloading cycles, we determined $E_{\text{three-point bending}}$ to be 12.7 ± 1.3 GPa while the total sample porosity was 57 ± 2 vol% as determined using gravimetrics.

Nanoindentation

Inorganic calcite single crystal

To establish a baseline for the material properties of the sea urchin spine basic material, we performed DSI measurements on a large calcite single crystal ($20 \times 20 \times 10$ mm^3). For a better comparability, we performed nanoindentation tests with $F_{\max} = 100$ mN in addition to DSI measurements with $F_{\max} = 15$ mN which yielded the very same results within the experimental error. Also, we did not find any influence of sample mounting for dense, solid calcite single crystal: both H_{IT} and E_{IT} were the same within the experimental error for calcite embedded in a resin block and for a calcite single crystal that was measured directly without any additional mount.

Figure 1 depicts a typical loading–unloading plot of calcite, which was also observed for all DSI measurements carried out on sea urchin spines. The discontinuities along the loading curve are caused by slip plane gliding as seen from the microphotograph in Fig. 1.

All measurements were carried out on the {1010} plane of a clear, natural calcite single crystal (Island). Based on 15 indentation measurements, we obtained 76.6 ± 1.9 GPa for the indentation modulus E_{IT} and 1.9 ± 0.1 GPa for the indentation hardness H_{IT}. Our measured E_{IT} is in agreement with DSI values reported for inorganic calcite in the literature (Ref. [24]: 73.5 ± 2.9 GPa/Ref. [10]: 78.1 ± 5.2 GPa) and slightly below the value reported by Griesshaber et al. (Ref. [25]: 85.0 GPa).

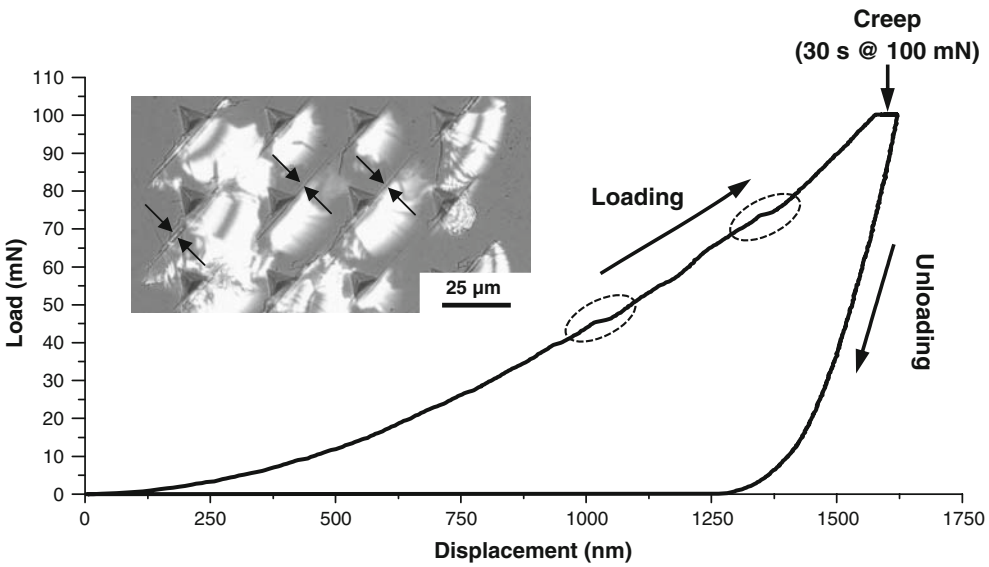

Fig. 1 Typical load–displacement plot for single crystal calcite. In the loading domain, small discontinuities (*dashed areas*) are results of slip plane gliding and crack formation in the brittle single crystal (*arrows in the inset*)

The H_{IT} value is, as expected, larger than the hardness determined via microindentation (Ref. [10]: 1.5 ± 0.1 GPa) and in agreement with H_{IT} values reported in the literature (Ref. [10]: 2.2 ± 0.2 GPa/Ref [24]: 2.7 ± 0.2 GPa). However, there are some substantially higher reported values (Ref. [26]: 3 GPa/Ref. [27]: 3.1–4.7 GPa/Ref. [25]: >3 GPa) which may be attributed to the range of material imperfections of natural inorganic calcite or different crystallographic orientations.

Sea urchin spines

Figure 2 displays cross sections of the measured sea urchin spine samples. The growth axis of the mesocrystalline calcite coincides with the crystallographic *c*-axis. For the displayed cross sections, the *c*-axis is perpendicular to the image plane. Characteristic features of the individual sea urchin spines are as follows:

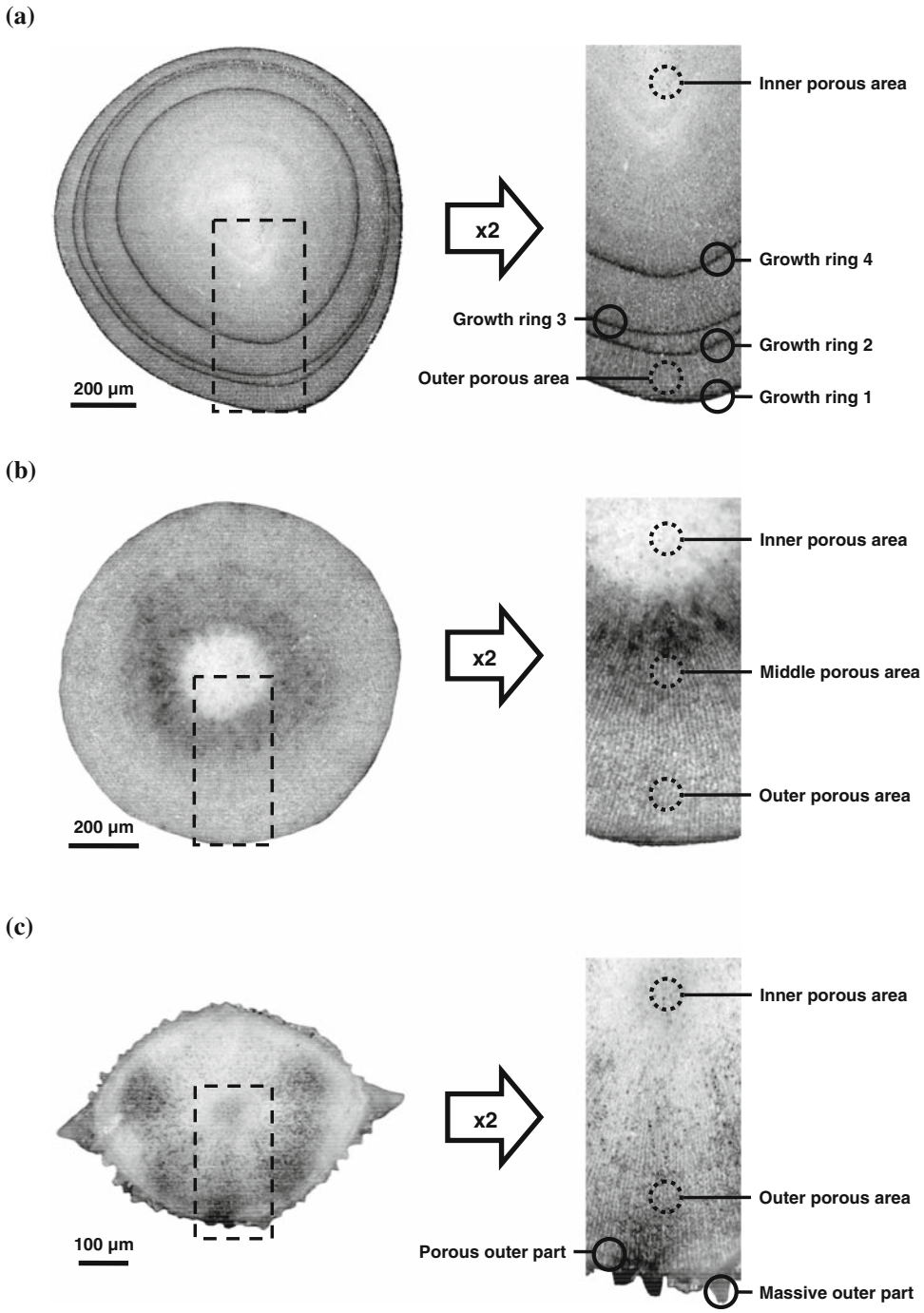

Fig. 2 Cross sections of the analyzed sea urchin spines of **a** *Heterocentrotus mammillatus*, **b** *Phyllacanthus imperialis*, and **c** *Prinocidaris baculosa*. Areas in which nanoindentation experiments were carried out are indicated and termed according to Table 1

- Spines of *Heterocentrotus mammillatus* are characterized by less porous parts which can be seen as former surfaces or growth marks. Measurements were carried out on each of the truncated growth rings as well as on the porous area between growth rings 1 and 2 ("outer porous area") and on the inner area (medulla = "inner porous area"). Porosity (Φ) ranges from relatively dense (growth rings: 15–20 vol%:) to highly porous (medulla: >50 vol%).
- Sea urchin spines of *Phyllacanthus imperialis* are less complex in their structure, and there is an almost continuous gradient of decreased porosity from the medulla ("inner porous area") to the outer rim of each cross section ("outer porous area"). Porosity levels show a less wide spread and range from 40 vol% (rim) to more than 65 vol% (medulla).
- For spines of *Prinocidaris baculosa* massive thorns on the outer rim are typical which lead to a structural differentiation between inner and outer spine areas. In the medulla, we find high porosity levels (>40 vol%) with a decreased porosity in stereom sections close to the rim (>30 vol%). The massive outer part is separated in the moderately porous inner part (≈25 vol%) and the almost fully dense outer part with massive thorns (<10 vol%).

The width of truncated trabeculae (i.e., the skeleton part of the structure) varies depending on the local porosity level as seen in Fig. 3. In highly porous areas, for example in the medulla of *Phyllacanthus imperialis*, the width of the trabecula can be below 10 μm, while massive growth rings show skeleton segments in the range of tens of micrometer. Locally even larger dense calcite portions were found in the part of *Prinocidaris baculosa*. As we examine random cross sections, it is, however, difficult to evaluate how thick a trabecula section extends into the depth. All indentations that were too close to or even in direct contact with the stereom–resin interface were removed from the data analysis.

First, we performed DSI measurements in static mode with a maximum load of 15 mN. This value is in the range of typical settings for DSI measurements of calcite [10, 21, 26–28] and corresponds to indentation depths of 500 nm. This value (0.5 μm) is a small fraction of the mean trabeculae diameter (≫5 μm). Figure 4 displays the results of the DSI measurements for indentation hardness and modulus illustrating the full spread of experimental values, while Table 1 lists the obtained mean values and standard deviations. All samples showed a similar variation in indentation hardness ranging from 2.5 to 5.0 GPa (average: 3.5 ± 0.5 GPa), independent from the studied sea urchin

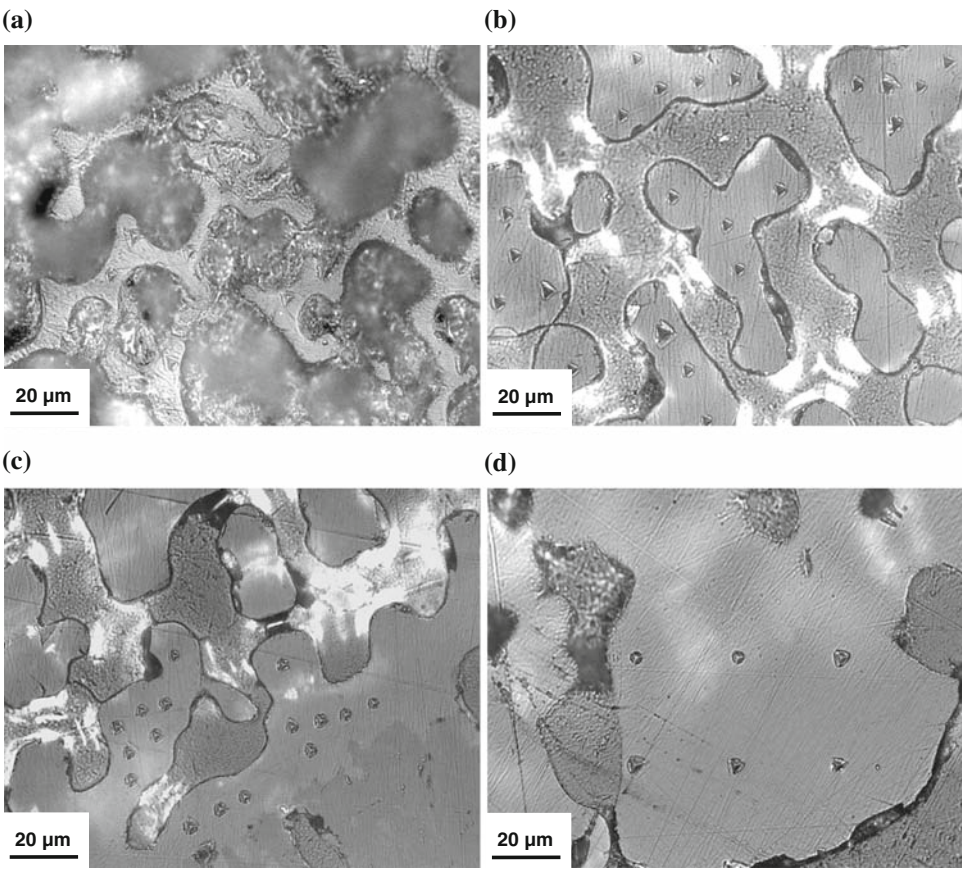

Fig. 3 Microphotographs of sea urchin spine samples after nanoindentation. Depending on the local porosity level, the width of trabeculae segments ranges from below 10 to more than 100 μm. **a** PI medulla (Φ > 60 vol%). **b** HM outer porous area (Φ > 30 vol%). **c** HM growth ring (Φ ≈ 20 vol%). **d** PB dense area (Φ < 10 vol%)

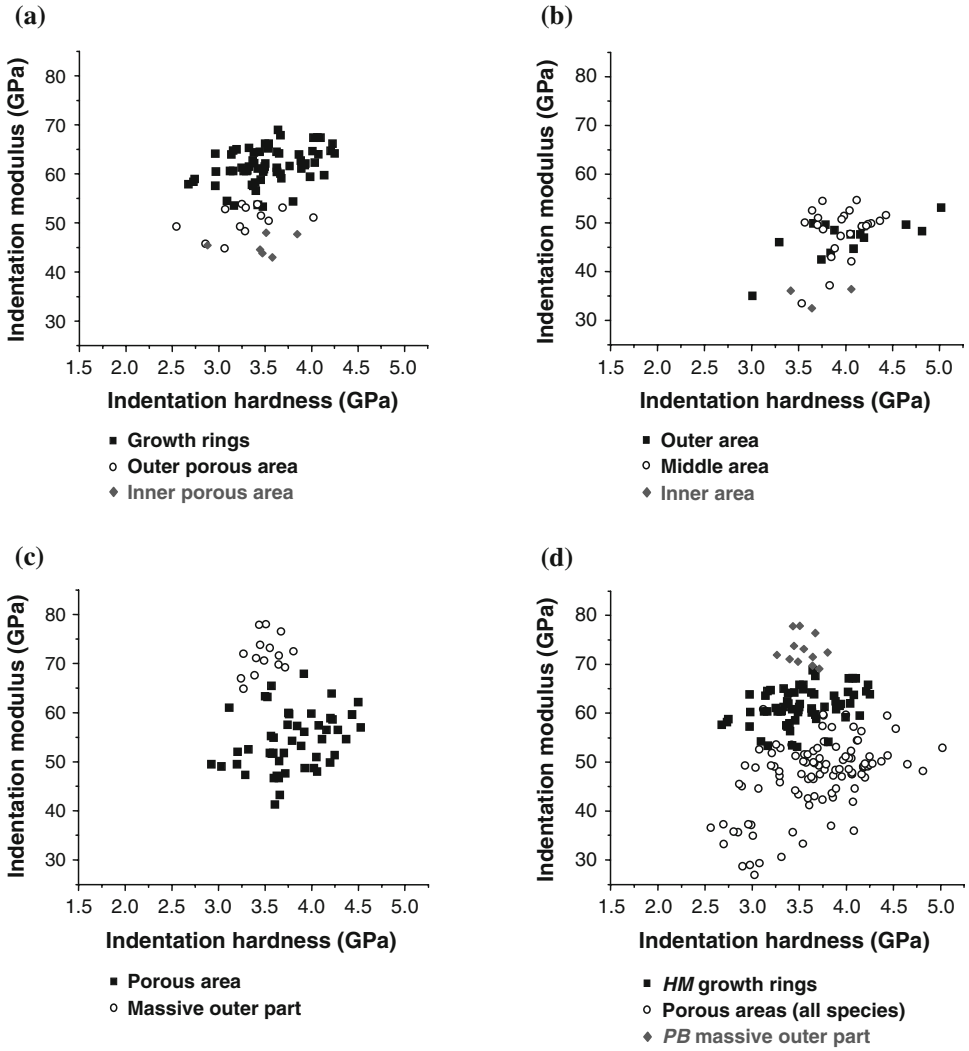

Fig. 4 DSI results for both, indentation hardness and modulus for **a** *Heterocentrotus mammillatus* (HM), **b** *Phyllacanthus imperialis* (PI), **c** *Prinocidaris baculosa* (PB), and **d** a plot showing all data (HM, PI, PB). For nomenclature see Fig. 3

species and the measured sample position (medulla, growth ring, etc.).

There is, however, a systematic variation of the indentation modulus: high values close to the E_{IT} of single crystal calcite (76.6 ± 1.9 GPa) were found in the massive part of *Prinocidaris baculosa* (71.7 ± 3.8 GPa). Also, relatively high indentation moduli were observed in the porous outer part of PB (59.1 ± 5.0 GPa) and in growth ring areas of *HM* (Ø: 61.7 ± 3.6 GPa). These values are opposed by a significantly decreased indentation modulus in areas with high porosity. In the medulla of *Phyllacanthus i*mperialis, for example, a very low E_{IT} value of 28.9 ± 5.8 GPa was found.

The values as determined from single crystal calcite cannot directly be compared with the results from sea urchin spines because of the different crystallographic orientation: while the single crystal was probed on its {1010} plane, the sea urchin spines were analyzed on the (0001) plane. Based on the elastic constants presented by Thanh and Lacam (Ref. [29]) and Yamamoto et al. (Ref. [30]), $E_{(0001)}$ varies between 75.5 and 85.3 GPa and thus coincides with our own DSI measurements on {1010} single crystal calcite (76.6 ± 1.9 GPa).

As a mean value, we obtain $H_{IT} = 3.5 \pm 0.5$ GPa for all analyzed samples. While this value is still in the range of reported values for natural inorganic calcite, the value is significantly higher than our measurements on single crystal calcite (1.9 ± 0.1 GPa). This may be due to the Mg-doping of the natural sea urchin calcite. Dolomite (50 mol% $MgCO_3$) has a significantly higher indentation hardness than pure calcite (Ref. [24]: 6.5 ± 0.9 GPa), but here the different crystal structure has to be taken into account. There is no systematic data on the indentation hardness of high magnesium calcite (hmc), but we know that sea urchin teeth (which show high amounts of Mg) show a higher indentation hardness than pure, Mg-free calcite [24, 31].

In order to investigate the nature of the systematic variations of E_{IT}, we performed CSM measurements for HM and PB for smaller applied loads (1–20 mN; Fig. 5). Here

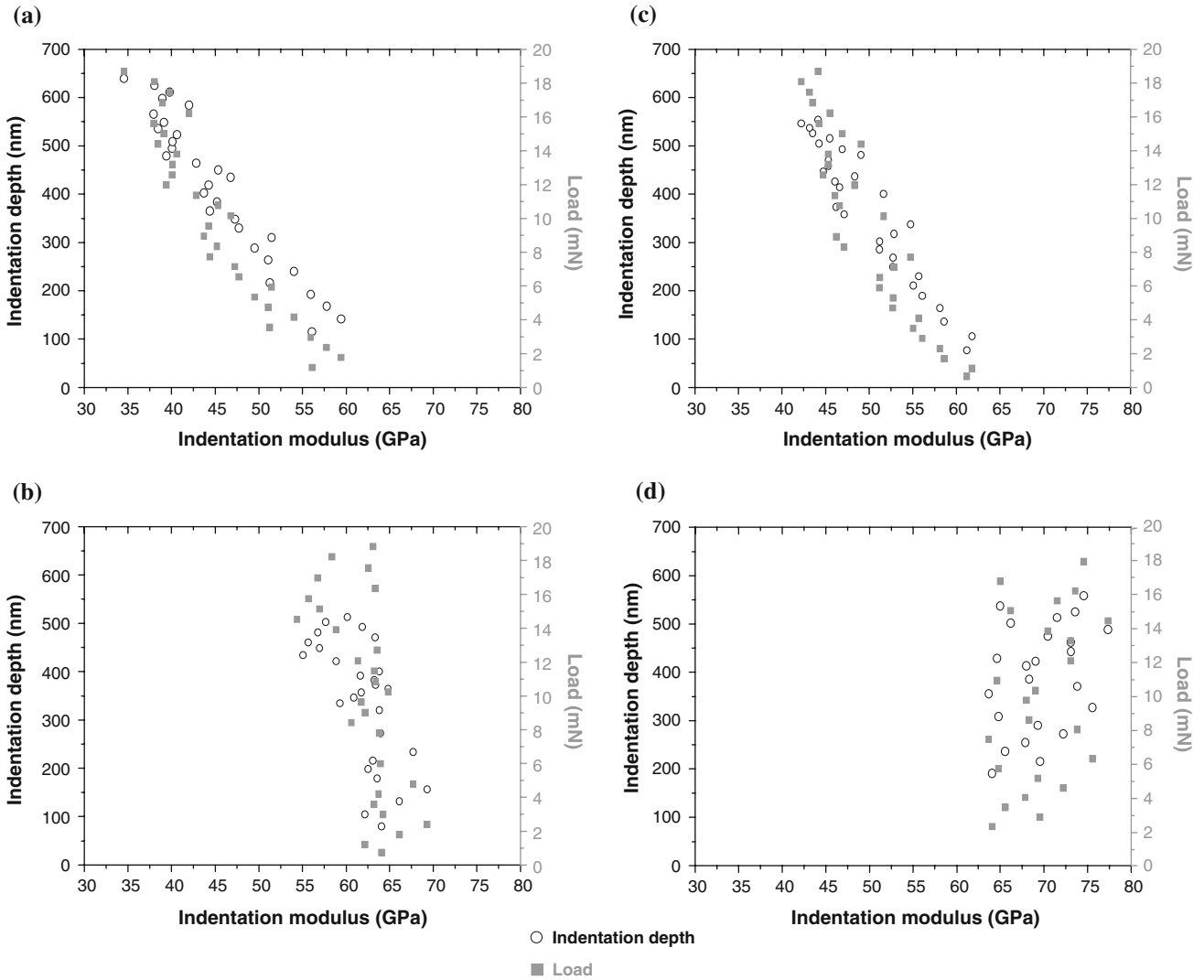

Fig. 5 CSM measurements showing the variation of E_{IT} with indentation depth and applied force. **a** HM: inner porous part ($\Phi \approx 61$ vol%). **b** HM: growth ring ($\Phi \approx 17$ vol%). **c** PB: inner porous part ($\Phi \approx 48$ vol%). **d** PB: massive outer part ($\Phi \approx 8$ vol%)

we see that the higher the resin volume fraction (= open pore volume), the larger the *z*-dependency of the indentation modulus. Only the almost dense massive outer part of *Prinocidaris baculosa* shows no significant variation of the indentation modulus with indentation depth and a constant indentation modulus of 68 ± 5 GPa can be calculated. Measurements in the inner porous part of PB yield the extrapolated value of 74 ± 19 GPa. For *Heterocentrotus mammillatus*, we obtain 63 ± 9 GPa ($\Phi = 61$ vol%) and 67 ± 5 GPa (17 vol%). Obviously, the indentation modulus of pure calcite is very close to the calculated E_{IT} values of sea urchin spine calcite. This aspect is very important, because it indicates that the organic component present within the stereom matrix does not influence the elastic modulus compared to inorganic single crystal calcite.

Because of the indentation size effect, it is known from thin film systems [20] and biological samples [32] that only for sufficiently low indentation loads/depths the true indentation modulus independent from (or, at least, only insignificantly affected by) the substrate/mounting can be obtained. In a recent study, Schmahl et al. (Ref. [33]) were able to study the variation of the elastic modulus of brachiopod shell caused by different levels of mineralization only after applying loads as small as 0.5 mN while a previous study (Ref. [34]) using 49 mN did not show any variation. Small indentation depths (e.g., 75 nm; Ref. [24]) and corresponding small indentation loads (e.g., 1 mN (Ref. [35]) or even 5 μN (Ref. [32])) can yield the true material indentation modulus but bring problems of their own. Using conventional mechanical–chemical sample preparation, the first tens of micrometer are often subject to structural deterioration with induced dislocations, amorphization, crack formation, and chemical alteration [36–38]. Such effects have to be considered and to be avoided if

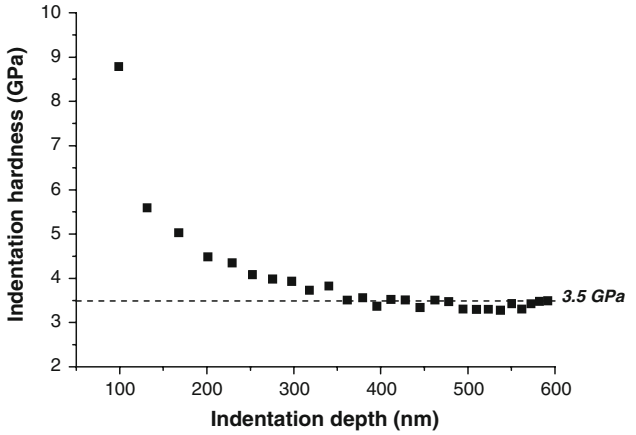

Fig. 6 CSM measurement (*PB*: massive outer part) showing the variation of H_{IT} with indentation depth. Similar results were obtained for all other samples

possible when applying nanoindenation with such small loads.

In fact, we observed that mechanical polishing and the corresponding strain hardening of the sample surface strongly influence the calculated indentation hardness at low indentation depths (Fig. 6). Strain hardening as a result of sample preparation significantly increases the H_{IT} at the very same small indentation depth where the "correct" indentation modulus of the calcite stereom can be obtained from.

Correlation between indentation modulus and local porosity

For a better understanding of the variation of E_{IT}, Fig. 7 plots the measured indentation modulus against the local porosity. The local porosity level was determined and the area 50 μm around the indentation was used for image analysis. As seen from the presented figures (Fig. 3) discrimination between calcite and resin was unambiguously possible with image analysis based on microscopic images. This approach of porosity determination is not as precise as other methods like gravimetrics, and we encountered a relative error of approximately 10%.

A clear trend of significantly decreased indentation modulus with increased porosity is plain from Fig. 7. It is linear in nature and thus corresponds to the Voigt model for composite materials: because of the resin infiltration, the pores are not empty and the infiltrated resin must be considered for the elastic behavior of the whole affected volume.

In the following calculation we assume that fully dense sea urchin calcite has the same elastic modulus as single crystal calcite and that the entire pore volume is fully infiltrated with the resin. Both assumptions are reasonable as the E_{IT} measurements in the massive thorn-decorated part of *Prinocidaris baculosa* are very close to the indentation modulus of single crystal calcite, and microscopic investigation shows that the entire pore volume is fully infiltrated by the resin.

There exist various models for the calculation of the mechanical properties of composite materials. The two most basic boundaries for the elastic modulus are given by the Reuss and Voigt equation [39]. While the Reuss model assumes an uniform stress for all components of the composite device, the Voigt model assumes an uniform strain. On the first glance, one might expect a Reussian relationship between the phase content of resin and the elastic modulus when indenting a calcite stereom pillar on

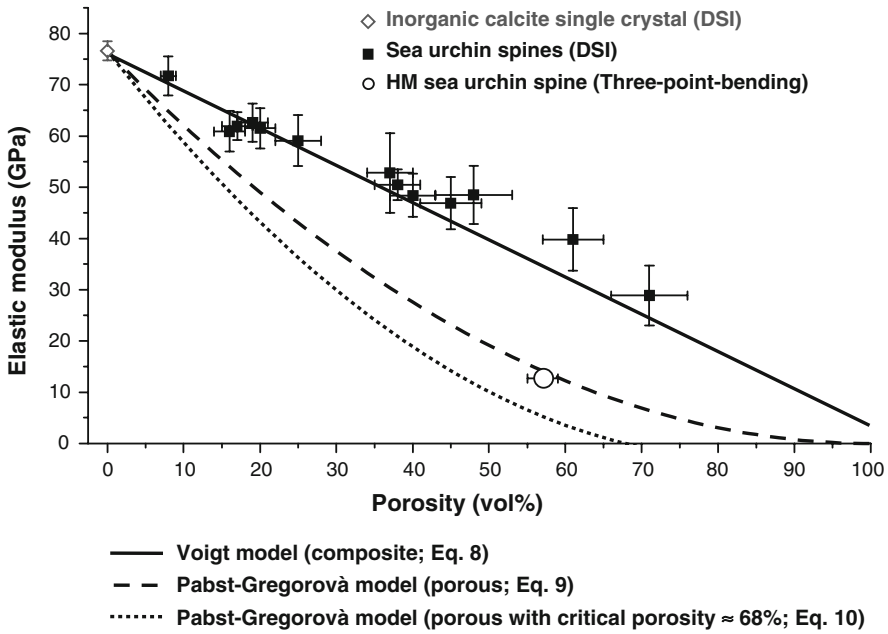

Fig. 7 Elastic modulus ($E_{\text{three-point bending}}$ and E_{IT}) versus sample porosity (three-point bending: global porosity/DSI: local porosity) and porosity–modulus models

top of resin, because the resin replaces pore space and appears as separated portions in sections. However, in the case of sea urchin spines we have two highly interconnected networks: the calcite stereom and the infiltrated resin. If the adhesion between resin and calcite is strong, both networks hinder each other in an individual response to stress and we end up with a constant strain behavior. In general, the reduced elastic modulus of cellular interconnected phase composites (IPC) lies in-between the Reuss and the Voigt boundary [7, 40].

For the spine stereom the reduced elastic modulus is best described by a Voigt correlation following Eq. 3 [39]:

$$E_{\text{composite}} = E_{\text{resin}} \cdot \Phi + E_{\text{calcite}} \cdot (1 - \Phi) \quad (3)$$

with $E_{\text{resin}} = 3.6$ GPa we obtain an excellent agreement between the measured indentation moduli and the calculated $E_{\text{composite}}$ values. A more detailed interpretation of the data with small E_{IT} or H_{IT} differences due to slight chemical changes may be possible, but is likely to be an over-interpretation of the data.

It is important, however, to note that because of the scatter of the data points and the experimental error a Reussian contribution of approximately 10% cannot be excluded. Figure 7 also shows the elastic modulus obtained with a traditional three-point bending test on a large HM spine segment. Here, the Voigt model does not apply: open pores cannot carry interface forces and hence a Reussian correlation between porosity and reduced elastic modulus is and must be observed. The porosity dependence of the elastic modulus is then described by equations of the Kingery–Coble-type Eq. 4 (for a review see Ref. [41])

$$E_{\text{porous body}} = E_{\text{fully dense body}} \cdot (1 - \Phi)^2 \quad (4)$$

The work of Pabst and Gregrovà [41] indicates that a critical porosity Φ_c may exist, above which a body loses structural integrity and cannot carry applied loads any longer [41–44]. When introducing this critical porosity, Eq. 4 transforms to Eq. 5 (Ref. [41]):

$$E_{\text{porous body}} = E_{\text{fully dense body}} \cdot (1 - \Phi) \cdot \left(1 - \frac{\Phi}{\Phi_c}\right) \quad (5)$$

For a number of ceramic bodies, a value of $\Phi_c = 68.4\%$ was found.

The value we obtained for $E_{\text{three-point bending}}$ plots in the area in-between Eqs. 4 and 5 assuming $E_{\text{calcite}} =$ 76.6 GPa. When examining the data point more closely, we see that the measured $E_{\text{three-point bending}}$ (12.7 GPa) value is closer to the value predicted from Eq. 4 ($\approx$ 14 GPa) than the elastic modulus obtained via Eq. 5 ($\approx$ 5 GPa) which assumes a critical porosity of 68.4%. The reason for this discrepancy is that for layered porous sea urchin spines the critical porosity is larger than 68.4%. In fact, we found areas exceeding 70 vol% local porosity.

As a result we note that for *both* three-point bending and nanoindentation on highly porous parts, we *do not necessarily* measure the mechanical properties of the trabeculae calcite made from calcite but the properties of the sampled volume as a system, in our case a composite of calcite and air or resin, respectively. Because the elastic field propagates far beyond the limits of the plastic deformation zone, this also applies for nanoindentation measurements. When applying smaller indentation loads, this effect can be minimized but needs to be considered depending on the actual size of the intended sampling volume. For bulk materials, simple models like the expanding cavity model (ECM; Ref. [45–47]) may be used to calculate the stress within the plastic and elastic zone (decreasing with a z^{-2} or z^{-3} depth dependency, respectively). For phase composites, such as highly interconnected phase composites, stress maps can be calculated using the finite element method (FEM) [48, 49]. The latter is beyond the scope of this manuscript, but Fig. 8 shows for the calcite stereom network only the von Mises stress distribution as caused by local indentation (using Catia V5 GPS, Dassault Systèmes, France). As seen, the stress encompassed the volume of several trabeculae which is in agreement with the chosen 50-μm distance for the calculation of the local sampling volume porosity.

Only by accurate data treatment using the Voigt model (DSI measurements on resin-infiltrated samples) or the model after Pabst and Gregorovà (three-point bending measurements on uninfiltrated samples) it is possible to calculate the actual elastic modulus of the bulk material or predict the effective modulus from a known value of a dense material.

In this study, we used the local porosity 50 μm around the indentation position as a measure for composite volume fraction of the mounting material. This corresponds to a

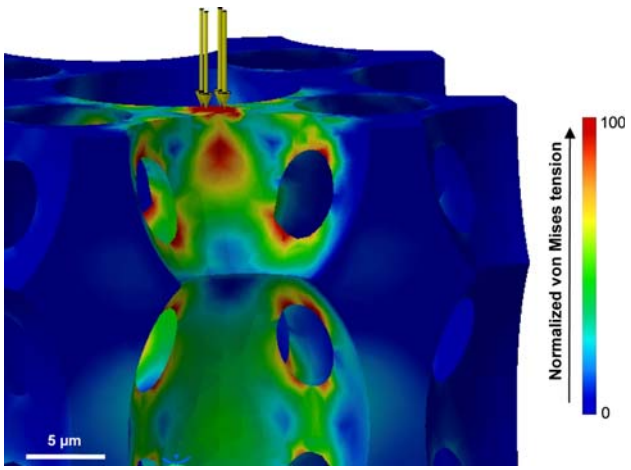

Fig. 8 FEM model of localized indentation within the calcite stereom and the resulting normalized von Mises tension

total volume of approximately 200 μm^3. Because of directional similarity (isotropy on a sub-mm level) of the stereom it is reasonable to assume that the porosity visible in the cross section is equal (or at least very similar) to the total porosity in this sampling volume. Although called *nano*indentation, it is, therefore, important to note that DSI often yields E_{IT} values that comprise at least *tens of cubic micrometers*. Only at very low indentation depths (sometimes referred to as ultra-nanoindentation) we may extract the correct indentation modulus for the calcite stereom.

Indentation hardness, however, seems not to be significantly affected by the mounting material. This is in agreement with the empirical 10% rule for thin film systems which states that as long as the indentation depth is ≤10% of the thin film thickness, the obtained indentation hardness is close to the intrinsic thin film hardness [4]. Only for very small indentation depths we find an increase in H_{IT} because of superficial strain hardening.

Conclusion

Sea urchin spines are characterized by strongly varying levels of local porosity, ranging from almost fully dense (*Prinocidaris baculosa* outer part) to pronouncedly porous (medulla of *Phyllacanthus imperialis*: >60 vol%). For large, fully dense bodies, such as a calcite single crystal, mounting the sample in resin has no significant effect on indentation modulus and an even smaller effect on the indentation hardness. Resin mounting can often not be avoided—especially when dealing with small and/or porous samples. Not only sample treatment (polishing) requires resin infiltration, but also DSI measurements using the CSM Nano-Hardness Tester® require a sample size of minimal 8 mm which, for smaller samples, can only be obtained when performing suitable sample mounting.

For porous samples, the presented data clearly indicates a macroscopic sampling volume of >100 μm^3 for the indentation modulus. The indentation hardness H_{IT} is not affected as this property is much more of local nature [1] and so the calculated values are those of sea urchin calcite. But this must not be mixed up with indentation modulus measurements, which need to be corrected for the amount and properties of mounting material in a much larger volume for the indentation depth studied in this article.

Literature (Ref. [25, 32, 33, 50]) shows, that applying loads ≤1 mN might be a possibility to overcome this implication. This, however, is not possible for all instruments or sample materials. Sample polishing is known to affect the very superficial part by introducing dislocations (resulting in strain hardening) and/or causing local amorphization. The scale for this effect lies in the tens of nanometer range (Ref. [36]), hence, potentially influencing DSI measurements with only a few nanometer indentation depth (500 μN load for mollusk calcite = 50–60 nm indentation depth; Ref. [34]). This especially applies for brittle materials with high elastic modulus (Ref. [36, 51, 52]).

For the calculated indentation modulus of resin-infiltrate sea urchin spine segments, a Voigtian relationship between the resin volume fraction on a 50-μm distance around the indentation spot and E_{IT} was found. This is because of the highly interconnected nature of the two network materials (resin and calcite, respectively) shifting the behavior from a Reussian to the observed Voigtian behavior. This may enable a new approach for tuning the mechanical properties of composites by rapidly lowering the elastic modulus as a result of decreasing the viscosity of the infiltration medium (hence, reducing the load-bearing capacity of the second network material and rendering the system rather Reussian).

Acknowledgements The authors gratefully acknowledge the funding of this study by the Landesstiftung Baden-Württemberg foundation as a part of the interdisciplinary project "New materials from bionics."

References

1. Vlassak JJ, Nix WD (1992) J Mater Res 7:3242
2. Doerner MF, Gardner DS, Nix WD (1986) J Mater Res 1:845
3. Chiu C-C, Liou Y, Juang Y-D (1995) Thin Solid Films 260:118
4. Fischer-Cripps AC (2004) Nanoindentation. Springer Verlag, Berlin
5. Asif SAS, Wahl KJ, Colton RJ (1999) Rev Sci Instrum 70:2408
6. Oliver WC, Pharr GM (1992) J Mater Res 7:1564
7. Sakai M (2009) J Mater Res 24
8. Nix WD, Gao H (1998) J Mech Phys Solids 46:411
9. Pharr GM, Strader JH, Oliver WC (2009) J Mater Res 24:635
10. Broz ME, Cook RF, Whitney DL (2006) Am Miner 91:135
11. Ma D, Ong CW, Wong SF (2005) J Mater Sci 40:2685. doi: 10.1007/s10853-005-2106-5
12. Presser V, Schultheiß S, Berthold C, Nickel KG (2009) J Bionic Eng 6:203
13. Presser V, Kohler C, Zivcova Z, Schultheiß S, Berthold C, Nickel KG, Pabst W, Gregorova E (2009) J Bionic Eng 6:357
14. O'Neill PL (1981) Science 213:646
15. Magdans U, Gies H (2004) Eur J Miner 16:261
16. Sethmann I, Putnis A, Grassmann O, Löbmann P (2005) Am Miner 90:1213
17. Sethmann I, Hinrichs R, Wörheide G, Putnis A (2006) J Inorg Biochem 100:88
18. Sethmann I, Wörheide G (2008) Micron 39:209
19. Berman A, Addadi L, Kvick A, Leiserowitz L, Nelson M, Weiner S (1990) Science 250:664
20. Din E (2007) Metallische Werkstoffe. Instrumentierte Eindringprüfung zur Bestimmung der Härte und anderer Werkstoffparameter. Teil 4: Prüfverfahren für metallische und nichtmetallische Schichten. Beuth Verlag, Berlin, p 31
21. Perez-Huerta A, Cusack M, Zhu W, England J, Hughes J (2007) J R Soc Interface 4:33
22. Delesse A (1848) Ann Miner 4:379

23. Rosiwal AK (1898) Verhandlungen der Geologischen Reichsanstalt Wien 1898:143
24. Ma Y, Cohen SR, Addadi L, Weiner S (2008) Adv Mater 20:1555
25. Griesshaber E, Schmahl WW, Neuser R, Pettke T, Blum M, Mutterlose J, Brand U (2007) Am Miner 92:722
26. Zügner S, Marquardt K, Zimmermann I (2006) Eur J Pharm Biopharmaceutics 62:194
27. Hangen UD (2001) Zeitschrift für Metallkunde 92:1074
28. Merkel C, Griesshaber E, Kelm K, Neuser R, Jordan G, Logan A, Mader W, Schmahl WW (2007) J Geophys Res Biogeosciences 112:G02008/1
29. Thanh DV, Lacam A (1984) Phys Earth Planet Interiors 34:195
30. Yamamoto A, Shiro Y, Murata H (1974) Bull Chem Soc Jpn 47:265
31. Wang RZ, Addadi L, Weiner S (1997) Philos Trans R Soc Lond B 352:469
32. Tai K, Dao M, Suresh S, Palazoglu A, Ortiz C (2007) Nat Mater 6:454
33. Schmahl WW, Griesshaber E, Merkel CK, Deuschle J, Neuser RD, Göetz AJ, Sehrbrock A, Mader W (2008) Miner Mag 72:541
34. Griesshaber E, Kelm K, Sehrbrock A, Job R, Schmahl WW, Mader W (2006) Mater Res Soc Sym Proc 898E:0898
35. Sachs C, Fabritius H, Raabe D (2006) J Mater Res 21:1987
36. Grim JR, Benamara M, Skowronski M, Everson WJ, Heydemann VD (2006) Semicond Sci Technol 21:1709
37. West GD, Perkins JM, Lewis MH (2004) J Mater Sci 39:6687. doi:10.1023/B:JMSC.0000045600.77776.08
38. Presser V, Berthold C, Wirth R, Nickel KG (2008) Curr Opin Solid State Mater Sci 12:73
39. Ashby MF (2004) Materials selection in mechanical design. Elsevier, Amsterdam
40. Liu Y, Gong X-I (2006) Trans Nonferrous Met Soc China 16:s439
41. Pabst W, Gregorova E, Ticha G (2006) J Eur Ceram Soc 26:1085
42. Gregorova E, Zivcova Z, Pabst W (2006) J Mater Sci 41:6119. doi:10.1007/s10853-006-0475-z
43. Pabst W, Gregorová E (2003) J Mater Sci Lett 22:959
44. Pabst W, Gregorova E (2004) J Mater Sci 39:3501. doi:10.1023/B:JMSC.0000026961.12735.2a
45. Ai A, Dai LH (2007) Scripta Mater 56:761
46. Galanov BA, Domnich V, Gogotsi Y (2002) Exp Mech 43:303
47. Gao X-L (2006) J Mater Res 21:1317
48. Wegner LD, Gibson LJ (2000) Int J Mech Sci 42:925
49. Wegner LD, Gibson LJ (2000) Int J Mech Sci 42:943
50. Tai K, Qi HJ, Ortiz C (2005) J Mater Sci Mater Med 16:947
51. Kikuchi M, Takahashi Y, Suga T, Suzuki S, Bando Y (1992) J Am Ceram Soc 75:189
52. Owman F, Hallin C, Martensson P, Janzen E (1996) J Cryst Growth 167:391